

TransCAR: Transformer-based Camera-And-Radar Fusion for 3D Object Detection

Su Pang, Daniel Morris, Hayder Radha
Michigan State University

pangsu@msu.edu, dmorris@msu.edu, radha@msu.edu

Abstract

Despite radar’s popularity in the automotive industry, for fusion-based 3D object detection, most existing works focus on LiDAR and camera fusion. In this paper, we propose TransCAR, a Transformer-based Camera-And-Radar fusion solution for 3D object detection. Our TransCAR consists of two modules. The first module learns 2D features from surround-view camera images and then uses a sparse set of 3D object queries to index into these 2D features. The vision-updated queries then interact with each other via transformer self-attention layer. The second module learns radar features from multiple radar scans and then applies transformer decoder to learn the interactions between radar features and vision-updated queries. The cross-attention layer within the transformer decoder can adaptively learn the soft-association between the radar features and vision-updated queries instead of hard-association based on sensor calibration only. Finally, our model estimates a bounding box per query using set-to-set Hungarian loss, which enables the method to avoid non-maximum suppression. TransCAR improves the velocity estimation using the radar scans without temporal information. The superior experimental results of our TransCAR on the challenging nuScenes datasets illustrate that our TransCAR outperforms state-of-the-art Camera-Radar fusion-based 3D object detection approaches.

1. Introduction

Radars have been used for Advanced Driving Assistance System (ADAS) for many years. However, despite radar’s popularity in the automotive industry, when considering 3D object detection most existing works focus on LiDAR [14, 23, 25, 26, 40–42, 45], camera [2, 7, 24, 35] and LiDAR-camera fusion [6, 11, 12, 15, 16, 21–23, 37, 38, 43]. One reason for this is that there are not as many open datasets annotated with 3D bounding boxes that include radar data [3, 5, 9, 29]. Another reason is that, compared to LiDAR point clouds,

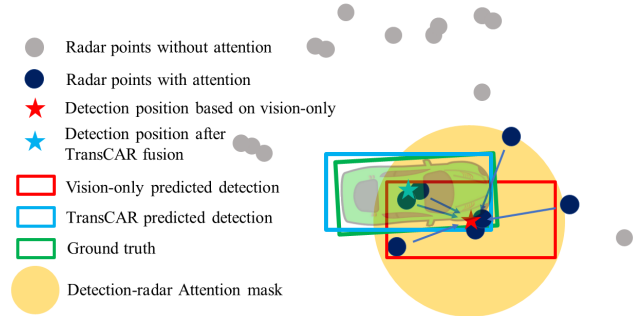


Figure 1: An example from nuScenes [3] showing how TransCAR fusion works. Vision-only detection has significant range error. Our TransCAR fusion can learn the interactions between vision-based query and related radar signals and predict improved detection. Unrelated radar points are prevented from attention by Query-Radar attention mask.

automotive radar signals are much sparser and lack height information. These properties make it challenging to distinguish between returns from objects of interest and backgrounds. However, radar has its strengths compared to LiDAR: (1) radar is robust under adverse weather and light conditions; (2) radar can accurately measure object’s radial velocity through the Doppler effect without requiring temporal information from multiple frames; (3) radar has much lower cost compared to LiDAR. Therefore, we believe there is a strong potential for performance gain by pursuing radar-camera fusion research.

3D object detection is essential for self-driving and ADAS systems. The goal of 3D object detection is to predict a set of 3D bounding boxes and category labels for objects of interest. It is challenging to directly estimate and classify 3D bounding boxes from automotive radar data alone due to its sparsity and lack of height information. Monocular camera-based 3D detectors [2, 7, 19, 24, 35] can classify objects, predict heading angles and azimuth angles of objects accurately. However, the errors in depth estimation are significant because regressing depth from a single

image is inherently an ill-posed inverse problem. Radar can provide accurate depth measurement, which monocular camera-based solutions cannot. Camera can produce classification and 3D bounding box estimation that radar-based solutions cannot. Therefore, it is a natural idea to fuse radar and camera for better 3D object detection performance.

Data association between different sensor modalities is the main challenge for sensor fusion technologies. Existing works mainly rely on multi-sensor calibration to do pixel-level [31], feature level [6, 12, 15, 16, 39] or detection level [21, 22] association. However, this is challenging for radar and camera association. First, the lack of height measurement in radar makes the radar-camera projection incorporate large uncertainties along the height direction. Second, radar beams are much wider than a typical image pixel and can bounce around. This can result in some hits visible to the radar but are occluded from the camera. Third, radar measurements are sparse and have low resolution. Many objects visible to the camera do not have radar hits. For these reasons, the hard-coded data association based on sensor calibration performs poorly for radar and camera fusion.

The seminal *Transformer* framework was initially proposed as a revolutionary technology for natural language processing (NLP) [30], and subsequently has shown its versatility in computer vision applications including object classification [8] and detection [4, 47]. The self-attention and cross-attention mechanism within the transformer can learn the interactions between multiple sets of information [1, 4, 30]. And we believe that this makes the transformer framework a viable fit to solve the data association in camera-radar fusion. In this paper, we propose a novel Transformer-based Radar and Camera fusion network termed TransCAR to address the problems mentioned above.

Our TransCAR first uses DETR3D [35] to generate image-based object queries. Then TransCAR learns radar features from multiple accumulated radar scans and applies a transformer decoder to learn the interactions between radar features and vision-updated queries. The cross-attention within the transformer decoder can adaptively learn the soft-association between the radar features and vision-updated queries instead of hard-association based on sensor calibration only. Finally, our model predicts a bounding box per query using a set-to-set Hungarian loss. Figure 1 illustrates the main idea of TransCAR. We also add the velocity discrepancy as a metric for the Hungarian bipartite matching because radar can provide accurate radial velocity measurements. Although our focus is on fusing multiple monocular cameras and radars, the proposed TransCAR framework is applicable to stereo camera systems as well. We demonstrate our TransCAR using the challenging nuScenes dataset [3]. TransCAR outperforms all other state-of-the-art (SOTA) camera-radar fusion-based methods

by a large margin. The proposed architecture delivers the following contributions:

- We study the characteristics of radar data and propose a novel camera-radar fusion network that adaptively learns the soft-association, and we show superior 3D detection performance compared to hard-association based on radar-camera calibration.
- We propose a novel camera-radar fusion network that adaptively learns the soft-association, and we show superior 3D detection performance compared to hard-association based on radar-camera calibration.
- The Query-Radar attention mask is proposed to assist the cross-attention layer to avoid unnecessary interactions between faraway vision queries and radar features, and in better learning the associations.
- TransCAR improves the velocity estimation using radar without requiring temporal information.
- At the time of submission, TransCAR ranks **1st** among published camera-radar fusion-based methods on the nuScenes 3D detection benchmark.

2. TransCAR

A high-level diagram of the proposed TransCAR architecture is shown in Figure 2. The camera network first utilizes surround-view images to generate vision-updated object queries. The radar network encodes radar point locations and extract radar features. Then the TransCAR fusion module fuses the vision-updated object queries with useful radar features. In the following, we present the details of each module in TransCAR.

2.1. Camera Network

Our camera network takes surround-view images collected by 6 cameras covering the full 360 degrees around the ego-vehicle and initial 3D object queries as input, and outputs a set of vision-updated 3D object queries in the 3D space. We apply DETR3D [35] to the camera network and follow the iterative top-down design. It utilizes initial 3D queries to index 2D features for refining 3D queries. The output 3D vision-updated queries are the input for the TransCAR fusion module.

2.1.1 Why Start from Camera

We use surround-view images to generate 3D object queries for fusion. Radar is not suitable for this task because many objects of interest do not have radar returns. There are two main reasons behind this. First, a typical automotive radar has a very limited vertical field of view compared to both camera and LiDAR, and it is usually installed at a lower

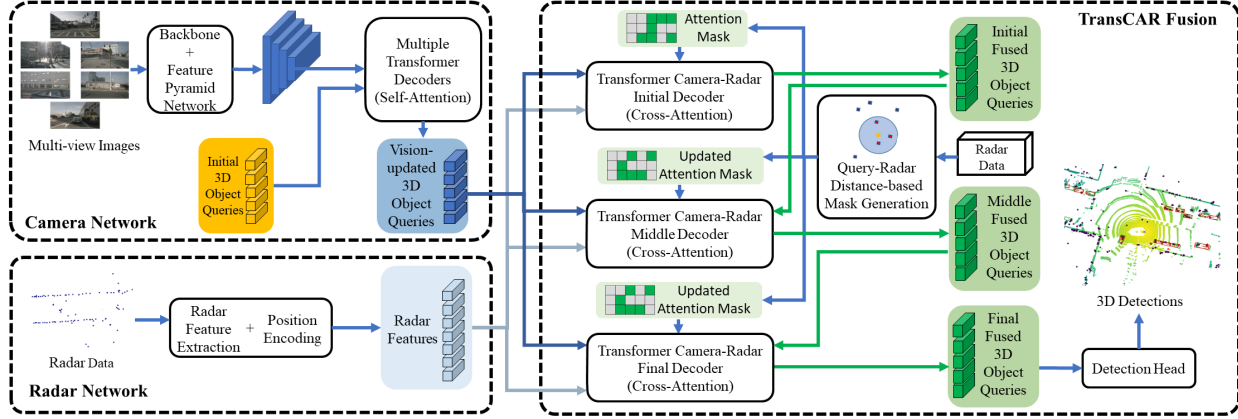


Figure 2: TransCAR system architecture. There are three primary components in the system: (1) A camera network (DETR3D [35]) based on transformer decoders to generate image-based 3D object queries. The initial object queries are generated randomly; (2) A radar network that encodes radar point locations and extracts radar features; (3) The TransCAR fusion module based on three transformer cross-attention decoders. We propose to use transformer to learn the interactions between radar features and vision-updated object queries for adaptive camera-radar association.

position. Therefore, any object that is located out of the radar’s small vertical field of view will be missed. Second, unlike LiDAR, the radar beams are wider and the azimuth resolution is limited, making it difficult to detect small objects. According to our statistics in supplementary materials, in the nuScenes training set, radar has a high miss rate, especially for small objects. For the two most common classes on the road, car and pedestrian, radar misses 36.05% of cars and 78.16% of pedestrians. Cameras have much better object visibilities. Therefore, we utilize images first to predict 3D object queries for fusion.

2.1.2 Methodology

The camera network uses ResNet-101 [10] with Feature Pyramid Network (FPN) [17] to learn a multi-scale feature pyramid. These multi-scale feature maps provide rich information for detecting objects in different sizes. Following [36, 47], our camera network (DETR3D [35]) is iterative. It has 6 transformer decoder layers to produce vision-updated 3D object queries; each layer takes the output queries from the previous layer as input. The steps within each layer are explained below.

For the first decoder layer, a set of N ($N = 900$ for nuScenes) learnable 3D object queries $Q^0 = \{\mathbf{q}_1^0, \mathbf{q}_2^0, \dots, \mathbf{q}_N^0\} \in \mathbb{R}^C$ are initialized randomly within the 3D surveillance area. The superscript 0 represents the input query to the first layer, and the subscript is the index of the query. The network learns the distribution of these 3D query positions from the training data. For the following layers, the input queries are the output queries from the previous layer. Each 3D object query encodes a 3D center location

$\mathbf{p}_i \in \mathbb{R}^3$ of a potential object. These 3D center points are projected to the image feature pyramid based on the camera extrinsic and intrinsic parameters to sample image features via bilinear interpolation. Assuming there are k layers in the image feature pyramid, the sampled image feature $\mathbf{f}_i \in \mathbb{R}^C$ for a 3D point \mathbf{p}_i is the sum of sampled features across all k levels, C is the number of feature channels. A given 3D center point \mathbf{p}_i may not be visible in any camera image. We pad the sampled image features corresponding to these out-of-view points with zeros.

A Transformer self-attention layer is used to learn the interactions among N 3D object queries and generate attention scores. The object queries are then combined with the sampled image features weighted by the attention scores to form the updated object queries $Q^l = \{\mathbf{q}_1^l, \mathbf{q}_2^l, \dots, \mathbf{q}_N^l\} \in \mathbb{R}^C$, where l is the current layer. Q^l is the input set of queries for the $(l + 1)$ -th layer.

For each updated object query \mathbf{q}_i^l , a 3D bounding box and a class label are predicted using two neural networks. The details of bounding box encoding and loss function are described in Section 2.4. A loss is computed after each layer during training. In inference mode, only the vision-updated queries output from the last layer are used for fusion.

2.2. Radar Network

The radar network is designed to learn useful radar features and encode their 3D positions for fusion. We first filter radar points according to x and y range, since only objects within $+/- 50$ meters box area in BEV are evaluated in nuScenes [3]. As radar is sparse, we accumulate radar from the previous 5 frames and transform them into the current frame. The nuScenes dataset provides 18 channels for each

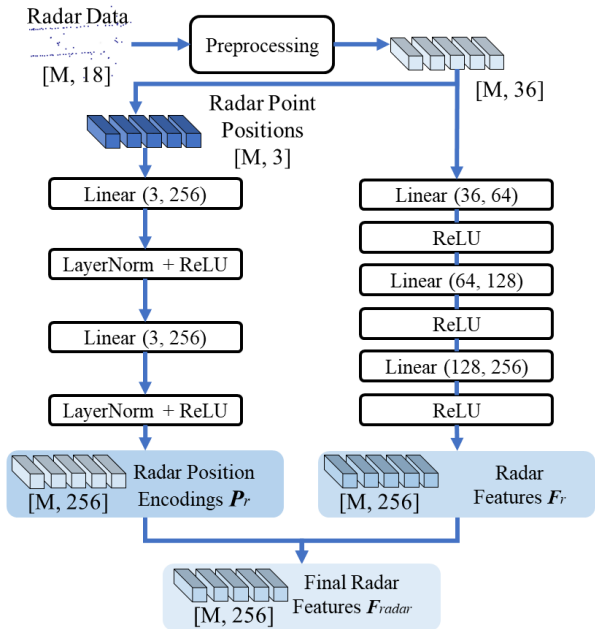


Figure 3: Details of radar network. The position encoding network (left) takes radar point positions (xyz) as input. The radar data after preprocessing (Section 2.2) are sent to the radar feature extraction network (right) to learn useful radar features. Since radar signal is very sparse, each radar point is treated independently. The numbers within the square brackets represent the shape of the data.

radar point, including the 3D location x, y, z in ego vehicle frame, radial velocities v_x and v_y , ego vehicle motion compensated velocities v_{xc} and v_{yc} , false alarm probability $pdh0$, a dynamic property channel $dynProp$ indicating whether or not the cluster is moving or stationary, and other state channels¹. To make the state channels feasible for the network to learn, we transform them into one-hot vectors. Since we use 5 accumulated frames, the time offset of each frame with regard to the current timestamp is useful to indicate the position offset, so we also add a time offset channel for each point. With these pre-processing operations, each input radar point has 36 channels.

Multilayer perceptron (MLP) networks are used to learn radar features $F_r \in \mathbb{R}^{M \times C}$ and radar point position encodings $P_r \in \mathbb{R}^{M \times C}$, where M and C are the number of radar points and the number of feature channels, respectively. In this paper, we set $M = 1500$ and $C = 256$ for nuScenes dataset. Note that there are less than 1500 radar points for each timestep even after accumulation in nuScenes dataset. Therefore, we pad the empty spots with out-of-scope positions and zero features for dimension compatibility. Figure

¹A detailed explanation of each channel can be found at: https://github.com/nutonomy/nuscenes-devkit/blob/master/python-sdk/nuscenes/utils/data_classes.py.

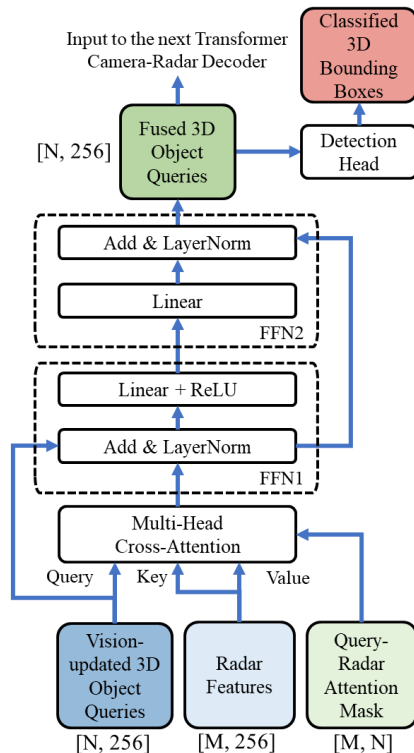


Figure 4: Details of transformer camera-radar decoder layer. The vision-updated 3D object queries are the queries to the multi-head cross attention module. The radar features are keys and values. See Section 2.3.2 for details. The numbers within the square brackets represent the shape of the data.

3 shows the details of the radar network. We combine the learned features and position encodings as the final radar features $F_{radar} = (F_r + P_r) \in \mathbb{R}^{M \times C}$. These final radar features together with the vision-updated queries from the camera network are used for TransCAR fusion in the next step.

2.3. TransCAR Fusion

TransCAR fusion module takes vision-updated queries and radar features from previous steps as input, and outputs fused queries for 3D bounding box prediction. Three transformer decoders work in an iterative fashion in the TransCAR fusion module. The query-radar attention mask is proposed to assist the cross-attention layer in better learning the interactions and associations between vision-updated queries and radar features.

2.3.1 Query-Radar Attention Mask

It is challenging and time consuming to train a transformer if both the number of input queries, keys and values are

large [4, 8]. For our transformer decoder, there are N 3D object queries $\mathbf{Q} \in \mathbb{R}^{N \times C}$ and M radar features $\mathbf{F}_{rad} \in \mathbb{R}^{M \times C}$ as keys and values, where $N = 900$ and $M = 1500$ for nuScenes. It is not necessary to learn every pairwise interaction (900×1500) between them. For a query $\mathbf{q}_i \in \mathbf{Q}$, only the nearby radar features are useful. There is no need to interact \mathbf{q}_i with other radar features that are far away. Therefore, we define a binary $N \times M$ Query-Radar attention mask $\mathbf{M} \in \{0, 1\}^{N \times M}$ to prevent attention for certain positions, where 0 indicates no attention and 1 represents allowed attention. A position (i, j) in \mathbf{M} is allowed for attention only when the xy Euclidean distance between the i -th query \mathbf{q}_i and the j -th radar feature \mathbf{f}_j is less than a threshold. There are three Query-Radar attention masks in TransCAR fusion corresponding to the three transformer decoders. The radii for these three masks are $2m$, $2m$ and $1m$, respectively.

2.3.2 Transformer Camera and Radar Cross-Attention

Three transformer cross-attention decoders are cascaded to learn the associations between vision-updated queries and radar features in our TransCAR fusion. Figure 4 shows the details of one transformer cross-attention decoder. For the initial decoder, the vision-updated queries $\mathbf{Q}_{img} \in \mathbb{R}^{N \times C}$ output from the camera network are the input queries. The radar features $\mathbf{F}_{rad} \in \mathbb{R}^{M \times C}$ are the input keys and values. The Query-Radar attention mask \mathbf{M}_1 is used to prevent attentions to certain unnecessary pairs. The cross-attention layer within the decoder will output an attention score matrix $\mathbf{A}_1 \in [0, 1]^{N \times M}$. For the M elements in the i -th row of \mathbf{A}_1 , they represent the attention scores between the i -th vision-updated query and all M radar features, and their sum is 1. Note that for each query, only radar features close to it are allowed for attention, so for each row in \mathbf{A}_1 , most of them are zeros. These attention scores are indicators of associations between vision-updated queries and radar features. Then, the attention-weighted radar features for vision-updated queries are calculated as $\mathbf{F}_{rad1}^* = (\mathbf{A}_1 \cdot \mathbf{F}_{rad}) \in \mathbb{R}^{N \times C}$. These weighted radar features combined with the original vision-updated queries are then augmented by a feed-forward network (FFN) Φ_{FFN1} . This forms the fused queries for initial-stage: $\mathbf{Q}_{f1} = \Phi_{FFN1}(\mathbf{Q}_{img} + \mathbf{F}_{rad1}^*) \in \mathbb{R}^{N \times C}$.

The middle and final transformer decoders work similarly to the initial one. But they take the previous fused queries \mathbf{Q}_{f1} instead of the vision-updated queries as input. Taking the middle query as an example, the new Query-Radar attention mask \mathbf{M}_2 is calculated based on the distance between \mathbf{Q}_{f1} and radar point positions. We also re-sample image features \mathbf{f}_{f2} using encoded query positions in \mathbf{Q}_{f1} as the query positions are updated in the ini-

tial decoder. Similarly to the initial decoder, the attention-weighted radar features for \mathbf{Q}_{f1} are defined as $\mathbf{F}_{rad2}^* = (\mathbf{A}_2 \cdot \mathbf{F}_{rad}) \in \mathbb{R}^{N \times C}$, where \mathbf{A}_2 includes the attention scores for initial-stage fused query \mathbf{Q}_{f1} and radar features \mathbf{F}_{rad} . The output fused queries are learned via $\mathbf{Q}_{f2} = \Phi_{FFN2}(\mathbf{Q}_{f1} + \mathbf{F}_{rad2}^* + \mathbf{f}_{f2}) \in \mathbb{R}^{N \times C}$. We apply two sets of FFNs after the two decoders to perform bounding box predictions. We compute losses from the two decoders during training, and only the bounding boxes output from the last decoder are used during inference.

Due to visibility limitations, some queries may have no nearby radar signals. These queries will not interact with any radar signals, and their attention scores are all zeros. Detections from these queries will be vision-based only.

2.4. Box Encoding and Loss Function

Box Encoding: We encode a 3D bounding box \mathbf{b}_{3D} as an 11-digit vector:

$$\mathbf{b}_{3D} = [\mathbf{cls}, x, y, z, h, w, l, \sin(\theta), \cos(\theta), v_x, v_y] \quad (1)$$

where $\mathbf{cls} = \{c_1, \dots, c_n\}$ is the class label, x, y and z are the 3D center location, h, w and l are the 3D dimension, θ is the heading angle, v_x and v_y are the velocities along the x and y axes. For each output object query \mathbf{q} , the network predicts its class scores $\mathbf{c} \in [0, 1]^n$ (n is the number of classes, $n = 10$ for nuScenes) and 3D bounding box parameters $\mathbf{b} \in \mathbb{R}^{10}$:

$$\mathbf{b} = [\Delta x, \Delta y, \Delta z, \log h, \log w, \log l, \sin(\theta), \cos(\theta), v_x, v_y] \quad (2)$$

where $\Delta x, \Delta y$ and Δz are the offsets between predictions and query positions from the previous layer. Different from DETR3D that estimates position offsets in the Sigmoid space [35], we directly regress the position offsets in the 3D Cartesian coordinates. DETR3D uses Sigmoid space because they want to keep the position outputs between $[0, 1]$, so all the queries positions are within the distance boundaries. While for TransCAR, we started from optimized vision-updated queries whose positions are relatively more accurate. Therefore, we can avoid the redundant non-linear activations which could potentially impact the learning.

Loss: We use a set-to-set Hungarian loss to guide training and measure the difference between network predictions and ground truths following [4, 28, 35]. There are two components in the loss function, one for classification and the other for bounding box regression. We apply focal loss [18] for classification to address the class imbalance, and $L1$ loss for bounding box regression. Assuming that N and K represent the number of predictions and ground truths in one frame, we pad ϕ (no object) with ground truths set since N is significantly larger than K . Following [4, 28, 35], we use Hungarian algorithm [13] to solve the bipartite matching

problem between the predictions and ground truths:

$$\hat{\sigma} = \underset{\sigma \in \Theta}{\operatorname{arg\,min}} \sum_i^N [-\mathbb{1}_{\{c_i \neq \phi\}} \hat{p}_{\sigma(i)}(c_i) + \mathbb{1}_{\{c_i \neq \phi\}} \mathcal{L}_{box}(\mathbf{b}_i, \hat{\mathbf{b}}_{\sigma(i)})] \quad (3)$$

where Θ denotes the set of permutations, $\hat{p}_{\sigma(i)}(c_i)$ represents the probability of class c_i with permutation index $\sigma(i)$, and \mathcal{L}_{box} is the $L1$ difference for bounding boxes, \mathbf{b}_i and $\hat{\mathbf{b}}_{\sigma(i)}$ are the ground truth box and predicted box respectively. Here, note that we also incorporate the velocity estimation v_x and v_y into \mathcal{L}_{box} for a better match and velocity estimation. With the optimal permutation $\hat{\sigma}$, the final Hungarian loss can be represented as follows:

$$\mathcal{L}_{Hungarian} = \sum_i^N [-\alpha(1 - \hat{p}_{\hat{\sigma}(i)}(c_i))^\gamma \log \hat{p}_{\hat{\sigma}(i)}(c_i) + \mathbb{1}_{\{c_i \neq \phi\}} \mathcal{L}_{box}(\mathbf{b}_i, \hat{\mathbf{b}}_{\hat{\sigma}(i)})] \quad (4)$$

where α and γ are the parameters of focal loss.

3. Experimental Results

We evaluate our TransCAR on the challenging nuScenes 3D detection benchmark [3] as it is the only open large-scale annotated dataset that includes radar.

3.1. Dataset

There are 6 cameras, 5 radars and 1 LiDAR installed on the nuScenes data collection vehicle. The nuScenes 3D detection dataset contains 1000 driving segments (scenes) of 20 seconds each, with 700, 150 and 150 segments for training, validation and testing, respectively. The annotation rate is 2Hz, so there are 28k, 6k and 6k annotated frames for training, validation and testing, respectively. There are 10 classes of objects. The true positive metric is based on BEV center distance.

3.2. Evaluation Results

We present our 3D detection results on the nuScenes test set in Table 1. Our TransCAR outperforms all other camera-radar fusion methods at the time of submission. Compared to the baseline camera-only method, DETR3D [35], TransCAR has higher mAP and NDS (nuScenes Detection Score [3]). Noted that DETR3D is trained with CBGS [46], while TransCAR is not. As shown in Table 1, among the 10 classes, the car class has the largest improvement (+2.4%). Cars and pedestrians are the main objects of interest in driving scenarios. In the nuScenes dataset, class Car has the highest proportion in the training set, it accounts for 43.74% of the total instances, and 63.95% of these car instances

have radar hits. Therefore, these car examples provide sufficient training examples for our TransCAR to learn the fusion. Class Pedestrian has the second highest proportion in the training set, it accounts for 19.67% of the total instances, but only 21.84% have radar returns. TransCAR can still improve pedestrian mAP by 1.2%. This demonstrates that, for objects with radar hits, TransCAR can leverage the radar hits to improve the detection performance, and for objects without radar hits, TransCAR can preserve the baseline performance.

Table 2 shows the quantitative comparison with baseline DETR3D [35] in Car class with different center distance evaluation metrics. In nuScenes dataset, the true positive metric is based on the center distance, which means the center distance between a true positive and the ground truth should be smaller than the threshold. nuScenes defines four distance thresholds ranging from 0.5 to 4.0 meters. As shown in Table 2, TransCAR improves the AP for all 4 metrics. In particular, for the more strict and important metrics 0.5 and 1.0 meters thresholds, the improvement is 5.84% and 6.19% respectively.

3.3. Qualitative Results

Figure 5 shows the qualitative comparison between TransCAR and baseline DETR3D [35] on the nuScenes dataset [3]. Blue and red boxes are the predictions from TransCAR and DETR3D respectively, green filled rectangles are ground truths. The larger dark points are radar points, smaller color points are LiDAR points for reference (color yellow to green indicates the increasing distance). The oval regions on the left column highlight the improvements made by TransCAR, the orange boxes on the image highlight the corresponding oval region in the top-down view. TransCAR can fuse the detections from baseline DETR3D and improve the 3D bounding box estimation significantly.

3.4. Ablation and Analysis

Due to space constraints, we show part of the ablation studies in this section, more ablation studies are shown in the supplementary materials.

Contribution of each component: We evaluate the contribution of each component within our TransCAR network. The ablation study results on nuScenes validation set are shown in Table 3. The vision-only baseline is DETR3D [35]. Radial velocity is one of the unique measurements that radar can provide; although it is not true velocity, it can still guide the network to predict the object’s velocity without temporal information. As shown in the second row of Table 3, without radar radial velocity, the network can only use the location of radar points for fusion, and the mAVE (m/s) is significantly higher (0.906 vs. 0.523). The Query-Radar attention mask can prevent attentions for certain pairs of queries and radar features based on their distances. With-

Method	Sensor	NDS↑	mAP↑	mAVE↓	Car	Truck	Bus	Trailer	C.V.	Ped.	Motor.	Bike	T.C.	Barrier
MonoDIS [27]	C	38.4	30.4	1.553	47.8	22.0	18.8	17.6	7.4	37.0	29.0	24.5	48.7	51.1
CenterNet [44]	C	40.0	33.8	1.629	53.6	27.0	24.8	25.1	8.6	37.5	29.1	20.7	58.3	53.3
FCOS3D [34]	C	42.8	35.8	1.434	52.4	27.0	27.7	25.5	11.7	39.7	34.5	29.8	55.7	53.8
PGD [33]	C	44.8	38.6	1.509	56.1	29.9	28.5	26.6	13.4	44.1	39.7	31.4	60.5	56.1
DETR3D [35] (baseline)	C	47.9	41.2	0.845	60.3	33.3	29.0	35.8	17.0	45.5	41.3	30.8	62.7	56.5
PointPillar [14]	L	45.3	30.5	0.316	68.4	23.0	28.2	23.4	4.1	59.7	27.4	1.1	30.8	38.9
infoFocus [32]	L	39.5	39.5	1.000	77.9	31.4	44.8	37.3	10.7	63.4	29.0	6.1	46.5	47.8
CenterFusion [20]	CR	44.9	32.6	0.614	50.9	25.8	23.4	23.5	7.7	37.0	31.4	20.1	57.5	48.4
TransCAR(Ours)	CR	52.2	42.2	0.495	62.7	33.6	30.0	36.0	17.9	46.7	43.1	32.2	62.9	57.0

Table 1: Quantitative comparison with SOTA methods on nuScenes test set. In ‘Sensor’ column, ‘C’, ‘L’ and ‘CR’ represent camera, LiDAR, and camera-radar fusion, respectively. ‘C.V.’, ‘Ped’, ‘Motor’ and ‘T.C’ are short for construction vehicle, pedestrian, motorcycle, and traffic cone, respectively. TransCAR is currently the best camera-radar fusion-based method with the highest NDS and mAP, and it even outperforms early-released LiDAR-based approaches. The best performers are highlighted in bold, excluding LiDAR-only solutions.

out it, each query has to interact with all the radar features (1500 in our work) within the scene. This is challenging for the network to fuse useful radar features with the query, resulting in poorer performance.

The iterative refinement: There are three transformer cross-attention decoders that work iteratively in TransCAR. We study the effectiveness of the iterative design in TransCAR fusion and present the results in Table 4. The quantitative results in Table 4 suggests that the iterative refinement in TransCAR fusion can improve the detection performance and is beneficial to fully leverage our proposed fusion archi-

Number of Transformer Decoders in TransCAR	mAP↑	NDS↑	mATE↓	mAVE↓
0 (Baseline, without fusion)	34.6	42.2	0.823	0.876
1	34.9	43.4	0.763	0.768
2	35.4	45.4	0.763	0.585
3	35.5	46.4	0.759	0.523

Table 4: Evaluation on detection results from different number of transformer decoders in TransCAR.

Methods	AP Car @0.5m	AP Car @1.0m	AP Car @2.0m	AP Car @4.0m
Baseline(DETR3D)	16.72	46.28	71.55	83.96
TransCAR	22.56	52.47	74.52	84.52
Improvement	+5.84	+6.19	+2.97	+0.56

Table 2: Average Precision (AP) comparison with baseline DETR3D in Car class with different center-distance evaluation metrics on nuScenes validation set. Our TransCAR improves the AP by a large margin in all evaluation metrics.

Method	mAP↑	NDS↑	mATE↓	mAVE↓
Vision-only Baseline [35]	34.6	42.2	0.823	0.876
w/o radar feature extraction	34.7	41.7	0.766	0.906
w/o Query-Radar attention mask	34.4	39.5	0.765	1.125
TransCAR(Ours)	35.5	46.4	0.759	0.523

Table 3: Ablation of the proposed TransCAR components on nuScenes val set.

ecture.

Performance in different distance ranges: Table 5 and Table 6 show the detection performance on nuScenes dataset in different distance ranges, Table 5 shows the average results for all the 10 classes, and Table 6 is for Car class only. The results from these two Tables suggest that the vision-only baseline method (DETR3D) and our TransCAR perform better in shorter distances. The improvements of TransCAR are more significant in the range of 20 – 40 meters. This is mainly because for objects within 20 meters, the position errors are smaller, there are limited space for leveraging radar for improvement. And for objects beyond 40 meters, the baseline performs poorly, therefore TransCAR can only provided limited improvement. Note that the mean average precision (mAP) and corresponding improvements for all 10 classes in Table 5 are smaller than the ones for Car class in Table 6. There are mainly two reasons for this. First, mAP is the mean of APs of all classes, in nuScenes dataset, radar sensor has a higher miss rate for small-sized object classes (ped, cyclist, traffic cone, etc.). For example, 78.16% of pedestrians and 63.74% of cyclists do not have radar returns. Therefore, the performances for these classes are worse compared to large-sized objects (car, bus, etc.). Therefore, the improvements brought by Tran-

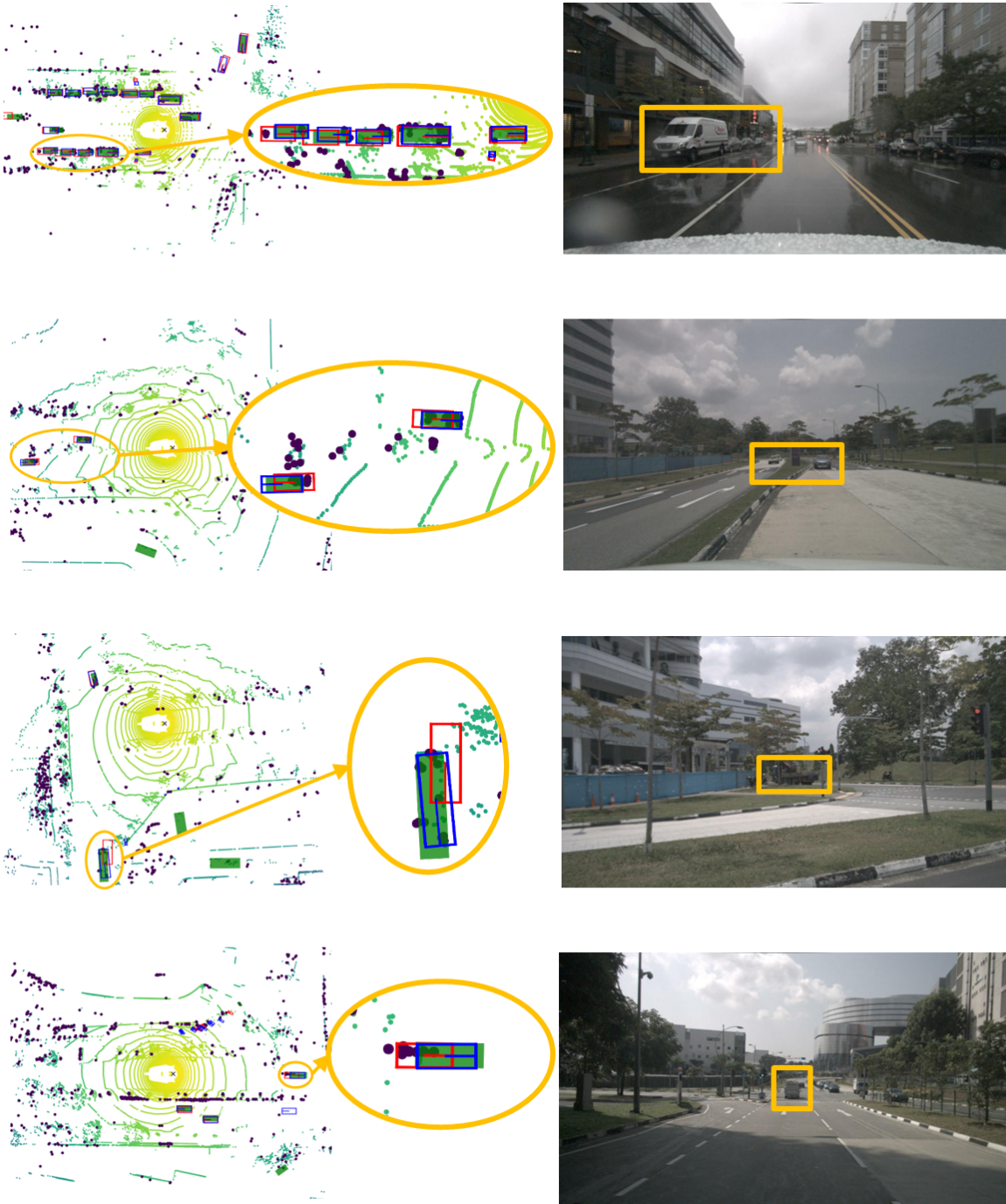


Figure 5: Qualitative comparison between TransCAR and baseline DETR3D on the nuScenes dataset [3]. Blue and red boxes are the predictions from TransCAR and DETR3D respectively, green filled rectangles are ground truths. The larger dark points are radar points, smaller color points are LiDAR points for reference (color yellow to green indicates the increasing distance). The oval regions on the left column highlight the improvements made by TransCAR, the orange boxes on the image highlight the corresponding oval region in the top-down view. Best viewed with zoom-in and color.

Method	All $\leq 20\text{m}$			All in 20 - 30m			All in 30 - 40m			All in 40 - 50m		
	mAP \uparrow	NDS \uparrow	mAVE \downarrow	mAP \uparrow	NDS \uparrow	mAVE \downarrow	mAP \uparrow	NDS \uparrow	mAVE \downarrow	mAP \uparrow	NDS \uparrow	mAVE \downarrow
DETR3D [35]	47.9	48.9	0.996	25.8	38.4	0.722	11.0	23.6	0.997	0.9	10.0	1.098
TransCAR (Ours)	48.6	54.0	0.537	26.6	41.9	0.450	11.9	27.4	0.705	1.0	10.8	0.938
Improvement	+0.7	+5.1	-0.459	+0.8	+3.5	-0.272	+0.9	+3.8	-0.292	+0.1	+0.8	-0.160

Table 5: Mean Average Precision (mAP, %), nuScenes Detection Score (NDS) and mean Average Velocity Error (AVE, m/s) for all classes of different distance ranges on nuScenes validation set. Our TransCAR outperforms the baseline (DETR3D) in all distance ranges.

sCAR for these classes are limited, for those classes of objects that have radar returns, TransCAR can leverage the radar signal to improve the detection performance, for the ones that do not have radar returns, TransCAR can only preserve the baseline performance. Second, there is a significant class imbalance in the nuScenes dataset, class Car accounts for 43.74% of the training instances, while for some other classes, such as class Cyclist and class Motorcycle only accounts for 1.00% and 1.07% respectively. The training examples for these rare classes are not sufficient. As for the major class Car, which is also the most common objects in the driving scenarios, TransCAR can improve the detection performance and velocity estimation by a large margin (Table 6).

Different weather and lighting conditions: Radar is more robust under different weather and light conditions compared to cameras. We evaluate the detection performance under rainy conditions and during the night, the results are shown in Table 7 and Table 8. Note that nuScenes does not provide the weather label for each annotated frame, the weather information is provided in the scene description section (a scene is a 20-second data segment [3]). After manual check of some of the annotated frames, we found that not all the frames under ‘rain’ were captured when the rain was falling, some of them were collected right before or after the rain. However, these images are of lower quality compared to the ones collected during sunny weather. Therefore, they are suitable for our evaluation experiments.

Table 7 shows the AP and AVE for class Car under rain and no-rain scenes. TransCAR has a higher AP improvement (+5.1% vs. +3.6%) for the rain scenes compared to no-rain scenes. The AVE for rain scenes is smaller than in the no-rain scenes; this is because there are biases in the rain frames, and the cars within these rain scenes are closer to the ego vehicle, which makes them easier to be detected.

Table 8 shows the comparison of the detection performance of night and daytime scenes. Poor lighting conditions at night make the baseline method perform worse than daytime (52.2% vs. 54.8% in AP, 1.691m/s vs. 0.866m/s in AVE), TransCAR can leverage the radar data and boost the AP by 6.9% and reduce AVE by 1.012m/s. Although there are limited night scenes (15 scenes, 602 frames), this

result can still demonstrate the effectiveness of TransCAR in night scenarios.

4. Supplementary Materials

4.1. Comparison of Radar and LiDAR Miss Rate

Compared to LiDAR, Radar has much higher miss rate. There are mainly two reasons: First, Automotive radar has a very limited field of view compared to LiDAR. And radar is usually installed at a lower position. Therefore, any object that is located out of the radar’s small vertical field of view will be missed. Second, radar beams are wider and the azimuth resolution is limited, making it difficult to detect small objects. The statistics of LiDAR and radar miss rate for nuScenes training set are shown in Table 9. We counted the number of objects in different classes, the number of objects missed by radar or LiDAR and the corresponding miss rate. Radar has a high miss rate, especially for small objects. For the two most common classes on the road, car and pedestrian, radar misses 36.05% of cars and 78.16% of pedestrians.

Note that we are not criticising radar. Table 9 shows the challenges of using radar for object detection tasks. Understanding the properties of radar measurements help us to design a reasonable fusion system. As discussed in the main paper, based on these statistics, we conclude that radar, as configured on the nuScenes vehicle, is not suitable to be used to generate the 3D queries.

We note that despite these physical limitations on the radar sensors, our results show that fusion with radar can significantly improve image-only detection. This opens the possibility of configuring radar differently, such as on the vehicle roof, to reduce the miss rate and potentially improve fusion performance further.

4.2. More Results on Secondary Evaluation Metrics

For completeness, we present Table 10 to show the comparison with other SOTA methods in other secondary evaluation metrics on the nuScenes test set. After fusing with radar, compared with other methods, our TransCAR has either better or same level of performance in all of the secondary evaluation metrics. In particular, with the fusion

Method	Cars $\leq 20m$		Cars in 20 - 30m		Cars in 30 - 40m		Cars in 40 - 50m	
	Radar Miss 31.53%		Radar Miss 73.29%		Radar Miss 48.16%		Radar Miss 50.45%	
	AP \uparrow	AVE \downarrow	AP \uparrow	AVE \downarrow	AP \uparrow	AVE \downarrow	AP \uparrow	AVE \downarrow
DETR3D [35]	76.4	0.917	48.7	0.810	28.8	0.934	5.0	1.015
TransCAR (Ours)	79.2	0.487	53.8	0.398	33.9	0.588	6.0	0.698
Improvement	+2.8	-0.430	+5.1	-0.412	+5.1	-0.346	+1.0	-0.317

Table 6: Average Precision (AP, %) and Average Velocity Error (AVE, m/s) for Car class of different distance ranges on nuScenes validation set. We also present the miss rate of radar sensor for different distance ranges. A car missed by radar is defined as a car that does not have radar return. Our TransCAR improves the AP and reduces the velocity estimation error by a large margin in all distance ranges.

Method	Rain		No Rain	
	AP \uparrow	AVE \downarrow	AP \uparrow	AVE \downarrow
DETR3D [35]	54.2	0.675	54.7	0.965
TransCAR (Ours)	59.3	0.409	58.3	0.534
Improvement	+5.1	-0.266	+3.6	-0.431

Table 7: Comparison of Average Precision (AP) and Average Velocity Error (AVE, m/s) for class Car under the rain and no-rain scenes on nuScenes validation set. There are 1088 frames (27 scenes) among 6019 frames (150 scenes) in nuScenes validation set are annotated as rain. TransCAR can significant improve the detection performance and reduce the velocity estimation error under rainy conditions.

Method	Night		Daytime	
	AP \uparrow	AVE \downarrow	AP \uparrow	AVE \downarrow
DETR3D [35]	52.2	1.691	54.8	0.866
TransCAR (Ours)	59.1	0.679	58.4	0.500
Improvement	+6.9	-1.012	+3.6	-0.366

Table 8: Comparison of Average Precision (AP) and Average Velocity Error (AVE, m/s) for class Car during the night and daytime scenes on nuScenes validation set. There are 602 frames among 6019 frames in nuScenes validation set are collected during the night. TransCAR can leverage the radar data to significantly improve the performance and reduce the velocity estimation error during the night when the camera is affected.

of radar signals, TransCAR outperform other methods in velocity estimation by a large margin. Compared to baseline (DETR3D), TransCAR improves the performance in all evaluation metrics.

4.3. More Ablation Studies

Number of radar frames for fusion: We accumulate multiple radar frames with ego vehicle motion compensation for fusion as radar point clouds are sparse. We evaluate the impact of accumulating different number of radar frames, and the results are presented in Table 11 and Table 12. Table 11 shows the evaluation results for all 10

classes in the nuScenes validation set, and Table 12 is the result for car class only. Accumulating 5 radar frames provides the overall best results, while the velocity error mAVE is slightly lower for accumulating 10 frames. Accumulating more radar frames can give us a denser radar point cloud for fusion, but at the same time, more noise points will be included. Also, for fast moving objects, accumulating more radar frames will generate a longer “trail” as the object motion cannot be compensated at this stage. This could potentially harm the bounding box location estimation.

Attention mask radii: In our TransCAR fusion system, we apply circle attention masks for transformer decoders. The radii of the circle attention masks can be different for each transformer decoder. We test different circle attention mask radius combinations on the nuScenes validation set, and the results are shown in Table 13. As shown in the Table 13, all radius configurations can improve the 3D detection performance significantly. There is a trade-off between large and small attention masks. Large attention mask can increase the probability of incorporating the right radar features, especially for large objects, but the chances of including noise and radar features from other nearby objects are also higher. As for small attention mask, we are more certain the included radar features are good ones, but there is a higher chance that we may miss the right radar features. According to Table 13, $(2m, 2m, 1m)$ has the best overall performance. Larger radii at the beginning provides a higher chance for detections to capture right radar features. A smaller radius at the end is better for the final estimation refinement.

5. Conclusion

In this paper, we proposed TransCAR, an effective and robust Transformer-based Camera-And-Radar 3D detection framework that can learn a soft-association between radar features and vision queries instead of a hard-association based on sensor calibration. The associated radar features improve range and velocity estimation. Our TransCAR sets the new state-of-the-art camera-radar detection performance on the challenging nuScenes detection benchmark.

Class	#Total	#Radar Misses	Radar Miss Rate	#LiDAR Misses	LiDAR Miss Rate
Car	318157	114697	36.05%	14196	4.46%
Truck	47687	12779	26.80%	1134	2.38%
Bus	7451	1521	20.41%	42	0.56%
Trailer	12604	2413	19.14%	413	3.28%
C.V.*	8655	2611	30.17%	166	1.92%
Ped.*	139493	109026	78.16%	473	0.34%
Motor.*	9209	5197	56.43%	196	2.13%
Bike	8171	5208	63.74%	111	1.36%
T.C.*	78532	54622	69.55%	1140	1.45%
Barrier	115105	81464	70.77%	1828	1.59%

Table 9: Statistics of objects in different classes in nuScenes training set within 50 meters of the ego vehicle. * ‘C.V.’, ‘Ped’, ‘Motor’ and ‘T.C’ represent construction vehicle, pedestrian, motorcycle and traffic cone, respectively. An object that is missed by radar or LiDAR is defined as having no hit/return from that object. Radar misses more objects. For the two most common classes in autonomous driving applications, car and pedestrian, radar misses 36.05% cars and 78.16% pedestrians. Although nuScenes does not provide detailed visibilities of objects in the image, we believe that it is much higher than radar. Therefore, we use camera instead of radar to generate 3D object queries for fusion.

Method	Sensor*	mAP \uparrow	NDS \uparrow	mATE \downarrow	mAVE \downarrow	mASE \downarrow	mAOE \downarrow	mAAE \downarrow
MonoDIS [27]	C	30.4	38.4	0.738	1.553	0.263	0.546	0.134
CenterNet [44]	C	33.8	40.0	0.658	1.629	0.255	0.629	0.142
FCOS3D [34]	C	35.8	42.8	0.690	1.434	0.249	0.452	0.124
PGD [33]	C	38.6	44.8	0.626	1.509	0.245	0.451	0.127
DETR3D [35](baseline)	C	41.2	47.9	0.641	0.845	0.255	0.394	0.133
PointPillar [14]	L	30.5	45.3	0.517	0.316	0.290	0.500	0.368
infoFocus [32]	L	39.5	39.5	0.363	1.000	0.265	1.132	0.395
CenterFusion [20]	CR	32.6	44.9	0.631	0.614	0.261	0.516	0.115
TransCAR(Ours)	CR	42.2	52.2	0.630	0.495	0.260	0.384	0.121

*In Sensor column, C represents Camera-only. L stands for LiDAR-only, CR shows Camera and Radar fusion-based approaches.

Table 10: Comparison with other SOTA methods in other secondary evaluation metrics defined by nuScenes dataset on nuScenes test set. The best performers are highlighted in bold exclude LiDAR-only solutions

Number of accumulated radar frames	mAP \uparrow	NDS \uparrow	mATE \downarrow	mAVE \downarrow
0 (Baseline [35])	34.6	42.2	0.823	0.876
1	35.3	44.3	0.762	0.703
3	35.4	44.9	0.755	0.657
5	35.5	46.4	0.759	0.523
10	35.4	46.3	0.764	0.521

Table 11: Evaluation on *all classes* detection results from accumulating different number of radar frames for fusion.

Number of accumulated radar frames	mAP \uparrow	mATE \downarrow	mAVE \downarrow
0 (Baseline [35])	54.63	0.544	0.911
1	57.6	0.508	0.729
3	58.26	0.494	0.641
5	58.52	0.493	0.511
10	58.37	0.496	0.501

Table 12: Evaluation on *Car* detection results from accumulating different number of radar frames for fusion.

We hope that our work can inspire further research on radar-camera fusion and motivate using transformers for sensor

fusion.

Attention mask radii for 3 transformer decoders	mAP \uparrow	NDS \uparrow	mATE \downarrow	mAVE \downarrow
Baseline [35]	34.6	42.2	0.823	0.876
(2m, 2m, 2m)	35.2	46.4	0.761	0.512
(2m, 2m, 1m)	35.5	46.4	0.759	0.523
(3m, 2m, 1m)	35.3	45.1	0.759	0.630
(2m, 1m, 1m)	35.4	46.2	0.757	0.541
(1m, 1m, 1m)	35.4	45.1	0.758	0.643

Table 13: Comparison of different attention mask radii for each transformer decoder in our TransCAR.

References

- [1] Xuyang Bai, Zeyu Hu, Xinge Zhu, Qingqiu Huang, Yilun Chen, Hongbo Fu, and Chiew-Lan Tai. Transfusion: Robust lidar-camera fusion for 3d object detection with transformers. In *Proceedings of the IEEE/CVF Conference on Computer Vision and Pattern Recognition*, pages 1090–1099, 2022. 2
- [2] Garrick Brazil and Xiaoming Liu. M3d-rpn: Monocular 3d region proposal network for object detection. In *Proceedings of the IEEE International Conference on Computer Vision*, pages 9287–9296, 2019. 1
- [3] Holger Caesar, Varun Bankiti, Alex H Lang, Sourabh Vora, Venice Erin Liong, Qiang Xu, Anush Krishnan, Yu Pan, Giancarlo Baldan, and Oscar Beijbom. nuscenes: A multi-modal dataset for autonomous driving. In *Proceedings of the IEEE/CVF conference on computer vision and pattern recognition*, pages 11621–11631, 2020. 1, 2, 3, 6, 8, 9
- [4] Nicolas Carion, Francisco Massa, Gabriel Synnaeve, Nicolas Usunier, Alexander Kirillov, and Sergey Zagoruyko. End-to-end object detection with transformers. In *European conference on computer vision*, pages 213–229. Springer, 2020. 2, 5
- [5] Ming-Fang Chang, John Lambert, Patsorn Sangkloy, Jagjeet Singh, Slawomir Bak, Andrew Hartnett, De Wang, Peter Carr, Simon Lucey, Deva Ramanan, et al. Argoverse: 3d tracking and forecasting with rich maps. In *Proceedings of the IEEE Conference on Computer Vision and Pattern Recognition*, pages 8748–8757, 2019. 1
- [6] Xiaozhi Chen, Huimin Ma, Ji Wan, Bo Li, and Tian Xia. Multi-view 3d object detection network for autonomous driving. In *Proceedings of the IEEE Conference on Computer Vision and Pattern Recognition*, pages 1907–1915, 2017. 1, 2
- [7] Yongjian Chen, Lei Tai, Kai Sun, and Mingyang Li. Monopair: Monocular 3d object detection using pairwise spatial relationships. In *Proceedings of the IEEE/CVF Conference on Computer Vision and Pattern Recognition*, pages 12093–12102, 2020. 1
- [8] Alexey Dosovitskiy, Lucas Beyer, Alexander Kolesnikov, Dirk Weissenborn, Xiaohua Zhai, Thomas Unterthiner, Mostafa Dehghani, Matthias Minderer, Georg Heigold, Sylvain Gelly, et al. An image is worth 16x16 words: Transformers for image recognition at scale. *arXiv preprint arXiv:2010.11929*, 2020. 2, 5
- [9] Andreas Geiger, Philip Lenz, and Raquel Urtasun. Are we ready for autonomous driving? the kitti vision benchmark suite. In *2012 IEEE Conference on Computer Vision and Pattern Recognition*, pages 3354–3361. IEEE, 2012. 1
- [10] Kaiming He, Xiangyu Zhang, Shaoqing Ren, and Jian Sun. Deep residual learning for image recognition. In *Proceedings of the IEEE conference on computer vision and pattern recognition*, pages 770–778, 2016. 3
- [11] Tengpeng Huang, Zhe Liu, Xiwu Chen, and Xiang Bai. Ep-net: Enhancing point features with image semantics for 3d object detection. In *European Conference on Computer Vision*, pages 35–52. Springer, 2020. 1
- [12] Jason Ku, Melissa Mozifian, Jungwook Lee, Ali Harakeh, and Steven L Waslander. Joint 3d proposal generation and object detection from view aggregation. In *2018 IEEE/RSJ International Conference on Intelligent Robots and Systems (IROS)*, pages 1–8. IEEE, 2018. 1, 2
- [13] Harold W Kuhn. The hungarian method for the assignment problem. *Naval research logistics quarterly*, 2(1-2):83–97, 1955. 5
- [14] Alex H Lang, Sourabh Vora, Holger Caesar, Lubing Zhou, Jiong Yang, and Oscar Beijbom. Pointpillars: Fast encoders for object detection from point clouds. *Proceedings of the IEEE Conference on Computer Vision and Pattern Recognition*, 2019. 1, 7, 11
- [15] Ming Liang, Bin Yang, Yun Chen, Rui Hu, and Raquel Urtasun. Multi-task multi-sensor fusion for 3d object detection. In *Proceedings of the IEEE Conference on Computer Vision and Pattern Recognition*, pages 7345–7353, 2019. 1, 2
- [16] Ming Liang, Bin Yang, Shenlong Wang, and Raquel Urtasun. Deep continuous fusion for multi-sensor 3d object detection. In *Proceedings of the European Conference on Computer Vision (ECCV)*, pages 641–656, 2018. 1, 2
- [17] Tsung-Yi Lin, Piotr Dollár, Ross Girshick, Kaiming He, Bharath Hariharan, and Serge Belongie. Feature pyramid networks for object detection. In *Proceedings of the IEEE Conference on Computer Vision and Pattern Recognition*, pages 2117–2125, 2017. 3
- [18] Tsung-Yi Lin, Priya Goyal, Ross Girshick, Kaiming He, and Piotr Dollár. Focal loss for dense object detection. In *Proceedings of the IEEE international conference on computer vision*, pages 2980–2988, 2017. 5
- [19] Arsalan Mousavian, Dragomir Anguelov, John Flynn, and Jana Kosecka. 3d bounding box estimation using deep learning and geometry. In *Proceedings of the IEEE Conference on Computer Vision and Pattern Recognition*, pages 7074–7082, 2017. 1
- [20] Ramin Nabati and Hairong Qi. Centerfusion: Center-based radar and camera fusion for 3d object detection. In *Proceedings of the IEEE/CVF Winter Conference on Applications of Computer Vision*, pages 1527–1536, 2021. 7, 11
- [21] Su Pang, Daniel Morris, and Hayder Radha. Clocs: Camera-lidar object candidates fusion for 3d object detection. *2020 IEEE/RSJ International Conference on Intelligent Robots and Systems (IROS)*, 2020. 1, 2

- [22] Su Pang, Daniel Morris, and Hayder Radha. Fast-clocs: Fast camera-lidar object candidates fusion for 3d object detection. In *Proceedings of the IEEE/CVF Winter Conference on Applications of Computer Vision*, pages 187–196, 2022. [1](#), [2](#)
- [23] Charles R Qi, Wei Liu, Chenxia Wu, Hao Su, and Leonidas J Guibas. Frustum pointnets for 3d object detection from rgb-d data. In *Proceedings of the IEEE Conference on Computer Vision and Pattern Recognition*, pages 918–927, 2018. [1](#)
- [24] Cody Reading, Ali Harakeh, Julia Chae, and Steven L. Waslander. Categorical depth distributionnetwork for monocular 3d object detection. *CVPR*, 2021. [1](#)
- [25] Shaoshuai Shi, Chaoxu Guo, Li Jiang, Zhe Wang, Jianping Shi, Xiaogang Wang, and Hongsheng Li. Pv-rcnn: Point-voxel feature set abstraction for 3d object detection. In *CVPR*, 2020. [1](#)
- [26] Shaoshuai Shi, Xiaogang Wang, and Hongsheng Li. Pointrcnn: 3d object proposal generation and detection from point cloud. In *Proceedings of the IEEE Conference on Computer Vision and Pattern Recognition*, pages 770–779, 2019. [1](#)
- [27] Andrea Simonelli, Samuel Rota Buló, Lorenzo Porzi, Manuel López-Antequera, and Peter Kotschieder. Disentangling monocular 3d object detection. In *Proceedings of the IEEE/CVF International Conference on Computer Vision*, pages 1991–1999, 2019. [7](#), [11](#)
- [28] Russell Stewart, Mykhaylo Andriluka, and Andrew Y Ng. End-to-end people detection in crowded scenes. In *Proceedings of the IEEE conference on computer vision and pattern recognition*, pages 2325–2333, 2016. [5](#)
- [29] Pei Sun, Henrik Kretschmar, Xerxes Dotiwalla, Aurelien Chouard, Vijaysai Patnaik, Paul Tsui, James Guo, Yin Zhou, Yuning Chai, Benjamin Caine, et al. Scalability in perception for autonomous driving: Waymo open dataset. In *Proceedings of the IEEE/CVF Conference on Computer Vision and Pattern Recognition*, pages 2446–2454, 2020. [1](#)
- [30] Ashish Vaswani, Noam Shazeer, Niki Parmar, Jakob Uszkoreit, Llion Jones, Aidan N Gomez, Łukasz Kaiser, and Illia Polosukhin. Attention is all you need. *Advances in neural information processing systems*, 30, 2017. [2](#)
- [31] Sourabh Vora, Alex H. Lang, Bassam Helou, and Oscar Beijbom. Pointpainting: Sequential fusion for 3d object detection. In *Proceedings of the IEEE/CVF Conference on Computer Vision and Pattern Recognition (CVPR)*, June 2020. [2](#)
- [32] Jun Wang, Shiyi Lan, Mingfei Gao, and Larry S Davis. Infocus: 3d object detection for autonomous driving with dynamic information modeling. In *European Conference on Computer Vision*, pages 405–420. Springer, 2020. [7](#), [11](#)
- [33] Tai Wang, ZHU Xinge, Jiangmiao Pang, and Dahua Lin. Probabilistic and geometric depth: Detecting objects in perspective. In *Conference on Robot Learning*, pages 1475–1485. PMLR, 2022. [7](#), [11](#)
- [34] Tai Wang, Xinge Zhu, Jiangmiao Pang, and Dahua Lin. Fcos3d: Fully convolutional one-stage monocular 3d object detection. In *Proceedings of the IEEE/CVF International Conference on Computer Vision*, pages 913–922, 2021. [7](#), [11](#)
- [35] Yue Wang, Vitor Campagnolo Guizilini, Tianyuan Zhang, Yilun Wang, Hang Zhao, and Justin Solomon. Detr3d: 3d object detection from multi-view images via 3d-to-2d queries. In *Conference on Robot Learning*, pages 180–191. PMLR, 2022. [1](#), [2](#), [3](#), [5](#), [6](#), [7](#), [9](#), [10](#), [11](#), [12](#)
- [36] Yue Wang and Justin M Solomon. Object dgcnn: 3d object detection using dynamic graphs. *Advances in Neural Information Processing Systems*, 34, 2021. [3](#)
- [37] Zhixin Wang and Kui Jia. Frustum convnet: Sliding frustums to aggregate local point-wise features for amodal 3d object detection. In *IROS*. IEEE, 2019. [1](#)
- [38] Liang Xie, Chao Xiang, Zhengxu Yu, Guodong Xu, Zheng Yang, Deng Cai, and Xiaofei He. Pi-rcnn: An efficient multi-sensor 3d object detector with point-based attentive context fusion module. In *Proceedings of the AAAI Conference on Artificial Intelligence*, volume 34, pages 12460–12467, 2020. [1](#)
- [39] Danfei Xu, Dragomir Anguelov, and Ashesh Jain. Pointfusion: Deep sensor fusion for 3d bounding box estimation. In *Proceedings of the IEEE Conference on Computer Vision and Pattern Recognition*, pages 244–253, 2018. [2](#)
- [40] Yan Yan, Yuxing Mao, and Bo Li. Second: Sparsely embedded convolutional detection. *Sensors*, 18(10):3337, 2018. [1](#)
- [41] Zetong Yang, Yanan Sun, Shu Liu, Xiaoyong Shen, and Jiaya Jia. STD: sparse-to-dense 3d object detector for point cloud. *ICCV*, 2019. [1](#)
- [42] Tianwei Yin, Xingyi Zhou, and Philipp Krähenbühl. Center-based 3d object detection and tracking. *CVPR*, 2021. [1](#)
- [43] Jin Hyeok Yoo, Yecheol Kim, and Ji Song Kim. 3d-cvf: Generating joint camera and lidar features using cross-view spatial feature fusion for 3d object detection. [1](#)
- [44] Xingyi Zhou, Dequan Wang, and Philipp Krähenbühl. Objects as points. *arXiv preprint arXiv:1904.07850*, 2019. [7](#), [11](#)
- [45] Yin Zhou and Oncel Tuzel. Voxelnet: End-to-end learning for point cloud based 3d object detection. In *Proceedings of the IEEE Conference on Computer Vision and Pattern Recognition*, pages 4490–4499, 2018. [1](#)
- [46] Benjin Zhu, Zhengkai Jiang, Xiangxin Zhou, Zeming Li, and Gang Yu. Class-balanced grouping and sampling for point cloud 3d object detection. *arXiv preprint arXiv:1908.09492*, 2019. [6](#)
- [47] Xizhou Zhu, Weijie Su, Lewei Lu, Bin Li, Xiaogang Wang, and Jifeng Dai. Deformable detr: Deformable transformers for end-to-end object detection. In *International Conference on Learning Representations*, 2020. [2](#), [3](#)